Giant Plasmonic Enhancement of Chiroptical Properties by Anisotropic Gold Nanocrystals Grown In Situ in a Chiral Polymer

Shema R. Abraham, Jojo P. Joseph, B. Medini Rajapakse, Avisek Dutta, Rahul Kumar Das, Andrey Kuzmin, Alexander Baev, Luis Velarde, Paras N. Prasad,* and Mark T. Swihart*

Polymer-based chiral materials with exceptional optical activity can dramatically impact integrated chiral photonics due to the tunability of their optical responses coupled with ease of fabrication. Realizing these applications requires increasing the absorbance dissymmetry factor. Here, in situ, the synthesis of gold nanostars is introduced in a chiral polymer medium to produce chiral polymer-anisotropic plasmonic nanocrystal nanocomposites. The optimized nanocomposite shows a tenfold enhancement of dissymmetry factor, g_{abs} (up to 0.64) and a corresponding 46-fold augmented circular dichroism (CD) value upon annealing, relative to the annealed pure chiral polymer film. Moreover, the enhancement relative to the non-annealed polymer-gold nanostar nanocomposite is strikingly higher: a 35-fold increase in g_{abs} and a 4272-fold increase in CD. Based on computational analysis, it is concluded that the local plasmon field enhancement around the crevices and tips of nanostars is mainly responsible for the observed effect which is further supported by a signal enhancement in Surface Enhanced Raman Scattering (SERS). Thus, this study underscores the significant role of close-range plasmon interactions in altering the chiroptical response of nanocomposite materials and a practical pathway toward the realization of next-generation integrated photonics and optoelectronic circuitry with photon spin control.

1. Introduction

Linear and nonlinear optical interactions using photons with specific values of spin angular momentum (circular polarization) and orbital angular momentum (non-Gaussian beams with helical wavefront) provide an exciting direction that expands the scope of traditional photonics and quantum optics. When light endowed with spin and/or orbital angular momentum impinges on a chiral medium, the coupling of angular momentum to electronic motion becomes stereo-selective. This selectivity is manifested as two complementary phenomena upon interaction with light: circular dichroism (CD) which is stereo-selective absorption of left- and right-circularly polarized light (LCP and RCP, respectively) and circular birefringence or optical rotation (optical rotatory dispersion, ORD) defined by the rotation of the linear polarization of the incoming light as it passes through the chiral medium.[1] The values of CD and ORD, the macroscopic observables, are determined by microscopic rotational strength, R, and the thickness of the material. Ultrahigh values of R allow the use of very thin films in device applications, which has clear benefits in terms of cost, flexibility, and scalability. Moreover, the relative simplicity of R in terms of the constituting microscopic physical quantities at the quantum level and their classic analogs allows the rational design of systems with enhanced macroscopic properties. Experimentally, differential absorption of circularly polarized light at a particular frequency can be quantified by a CD signal or via the absorption dissymmetry factor (g-factor), $g_{abs} = 2 \times (A_L - A_R)/(A_L - A_R)$, where A_L and A_R denote the absorbance of left and right-circularly polarized light. The dissymmetry ratio is independent of the optical density and thickness of a spatially uniform sample, which facilitates direct comparison of chiroptical properties of different chiral media (see Table S1, Supporting Information).[2] Chirality has important technological implications in photonics and optoelectronics because chiral media, especially those that can be manufactured into good optical quality thin films, can form a basis for future integrated

S. R. Abraham, M. T. Swihart
Department of Chemical and Biological Engineering
University at Buffalo
SUNY, NY 14260, USA
E-mail: swihart@buffalo.edu

S. R. Abraham, J. P. Joseph, A. Dutta, R. K. Das, A. Kuzmin, A. Baev,
L. Velarde, P. N. Prasad, M. T. Swihart
The Institute for Lasers
Photonics and Biophotonics
University at Buffalo
SUNY, NY 14260, USA
E-mail: pnprasad@buffalo.edu

J. P. Joseph, B. M. Rajapakse, A. Dutta, R. K. Das, L. Velarde, P. N. Prasad
Department of Chemistry
University at Buffalo
SUNY, NY 14260, USA

**ADVANCED
SCIENCE NEWS**

www.advancedsciencenews.com

**ADVANCED
OPTICAL
MATERIALS**

www.advopticalmat.de

photonic circuitry. In addition, the coupling of electric and magnetic transition dipoles, which is responsible for chiroptic effects in molecular media, also leads to magneto-optic effects. Thus, producing a material with enhanced optical activity may also lead to a medium exhibiting an enhanced magneto-optic response (Faraday rotation). Even though chirality (or handedness) is ubiquitous in nature on both molecular and macro-scales[3] dissymmetry factors are extremely low in naturally occurring systems, making them essentially useless for technological applications. The need to design, based on fundamental understanding of light-matter interactions, and synthesize a system (whether organic, inorganic or hybrid) with chiroptical properties surpassing those of naturally occurring materials is thus an urgent need. In this context, chiral fluorene- and thiophene-based polymers have been the subject of intense research due to their excellent chiroptical and electronic properties, processability, and chemical versatility.[2a,4] The electronic properties of these semiconducting polymers make them suitable for use in photovoltaic cells, polymer light-emitting diodes (PLEDs), field-effect transistors (FETs) and spin filters.[4c,5]

One of the most effective means of enhancing the chiroptical response of chiral polymers is plasmonic enhancement through the incorporation of plasmonic nanodomains – nanosized crystals of noble metals, typically gold. It should, however, be noted, that admixing gold nanocrystals into a layer of conjugated polymer could adversely affect some optoelectronic properties of the conductive polymer. For example, charge transport may be altered by the introduction of trap sites. On the other hand, multiple photonics applications can greatly benefit from plasmonic enhancement, such as epsilon-near-zero and negative refractive index metamaterials, biosensing, and surface-enhanced Raman scattering. The use of achiral plasmonic nanocrystals to harness the benefits of localized surface plasmon resonance (LSPR), such as extreme electric field concentration and near-field coupling has been studied extensively.[1b,6] The basic approach has been blending pre-manufactured spherical nanoparticles or nanorods into the chiral polymer. Short-range interaction between the local electric field of surface plasmons and the molecular transition dipole moments amplifies microscopic rotational strength via an effective increase of the electric transition dipole moment, mutual re-orientation of the electric and magnetic transition dipole moments, and hybridization of molecular wavefunctions. Prior studies showed that the combined response from a molecule-nanocrystal complex results in the microscopic rotational strength modified as $R_{mol,\,NP} \sim \Im m[(\hat{P} \cdot \vec{\mu}_{ij}) \cdot \vec{m}_{ij}] + F(\vec{\mu}_{ij}, \vec{m}_{ij})$, where $\vec{\mu}_{ij}$ designates transition electric dipole between states i and j, $\vec{m}_{ij}$ is the magnetic transition dipole between the same states, $F(\vec{\mu}_{ij}, \vec{m}_{ij})$ is the electric field enhancement matrix, and $F(\vec{\mu}_{ij}, \vec{m}_{ij})$ is a term quantifying the optical absorption originating from induction of chiral currents within the nanocrystal.[7] The first term refers to the rotational strength of the complex when there is an overlap between the molecular and plasmon absorption bands, as is the case in this study. The second term is important when there is no such overlap (chirality transfer) and will therefore be omitted in further discussion. Note that the electric field enhancement matrix transforms to the identity matrix, $\hat{1}$, when the distance between the molecule and the nanocrystal is greater than

the surface plasmon evanescent field decay distance.[7] At a large length scale, involving many such nanocrystals, additional amplification can arise due to the dipole-dipole inter-particle interactions, especially when the nanocrystals are arranged in a helical fashion due to specific anchoring along the polymeric backbone.[8] Because the LSPR and corresponding local field enhancement vary with the metal crystal's size, shape, and type, the enhancement coming from the matrix $\hat{P}$ can be optimized by varying these factors. It is also worth noting that because both rotational strength and absorption experience a change through the electric field-induced enhancement, the g-factor expressed in terms of the microscopic rotational strength and molecular polarizability in the dipole approximation becomes $g_{abs} = \Im m[(\hat{P} \cdot \vec{\mu}_{ij}) \cdot \vec{m}_{ij}]/(|\hat{P} \cdot \vec{\mu}_{ij}|^2 + |\vec{m}_{ij}|^2)$. If one considers only the effective enhancement of the amplitude of the transition electric dipole moment, $\vec{\mu}_{ij}$, it appears that rotational strength (CD) and g-factor cannot both increase via the above-described mechanism: the denominator changes as a square of the enhancement matrix whereas the numerator has a linear dependence, which would lead to a decrease of g-factor when rotational strength increases. However, mutual re-orientation of the electric and magnetic transition dipole moments (an effective change of the angle between two vectors) may result in the numerator growing at a faster rate than the denominator and, hence, the CD and g-factor simultaneously increasing. In addition, the above formula, as derived in the first order of the multipole expansion of the induced polarization for isotropic distribution of chiral molecules, neglects higher-order contributions to the rotational strength. For example, the quadrupolar term, which is usually considered negligibly small, can become important in oriented systems and can experience a substantial plasmonic enhancement, given the anisotropy of plasmonic nanoinclusions leading to very high gradients of the local electric field.[9] It has been shown theoretically that nanostructures generating steep field gradients can greatly enhance CD coupled to a molecular quadrupole-allowed transition.[10]

Herein, we demonstrate an in situ approach to intimately embed nanocrystals in our previously reported chiral fluorene-thiophene block co-polymer,[5h] to ensure homogeneous distribution of the nanocrystals within the chiral polymer matrix and close contact between the polymer backbone and nanocrystals. In situ growth of anisotropic nanocrystals (nanostars) in the polymer assembly allowed us to drastically enhance the CD signal within the spectral range of overlapping absorption bands of the polymer and plasmonic nanocrystals. The presence of thiophene units in the PF8TTS monomer building block[5h,i] helps to anchor the gold nanocrystals to the polymer fibrils. In what follows, we compare the chiroptical properties of neat PF8TTS polymer (hereafter P*) with PF8TTS-Au nanoparticle hybrid nanocomposite (P*AuNPs) and PF8TTS-Au nanostar hybrid nanocomposite (P*AuNSs) thin films and show the superior performance of the P*AuNSs system. Our experimental observations and conclusions are further supported by full-wave finite-element analysis of the plasmon field of Au nanostars. The presence of crystalline AuNSs and the close interaction of the polymer with them were confirmed by X-ray Diffraction (XRD), Raman, and X-ray Photoelectron Spectroscopy (XPS) analysis.

**ADVANCED
SCIENCE NEWS**

www.advancedsciencenews.com

**ADVANCED
OPTICAL
MATERIALS**

www.advopticalmat.de

2. Experimental Section

2.1. Materials Used for the Synthesis

Materials and methods for the polymer synthesis were described previously.[5h,i] Additional materials used here were tetra-*n*-octyl ammonium bromide (TOAB), >98% purity from TCI America, tetrachloroauric (III) acid (HAuCl$_4$.3H$_2$O), 99% pure from Millipore Sigma, sodium borohydride (NaBH$_4$), ≥98% purity from Millipore Sigma, oleylamine, ≥98% (primary amine) from Millipore Sigma, toluene (ACS Reagent) from Fisher Chemical, distilled (DI) water, copper (I) chloride (CuCl), ≥99.995% trace metals basis from Millipore Sigma, and ethanol, 200 proof (100%) from Decon Laboratories. These materials were used as received. The adhesion slides used for AFM imaging were from Statlab (Millenia 1000).

2.2. Characterization Techniques Used for the Analysis

All optical studies (Polarized Optical Microscopy (POM), SERS, Raman) and Atomic Force Microscopy (AFM) analysis were done on films coated on glass substrates. The Scanning Electron Microscopy (SEM) analysis was done on films coated on silicon substrates. The films were spin-coated on the substrates and further annealed in a Lindberg Blue M furnace in an inert atmosphere. The CD, UV-Vis, Optical Rotatory Dispersion (ORD) spectra and dissymmetry ratio studies were conducted on a JASCO J-1700 CD spectrophotometer (scanning rate of 100 nm min^{-1}, bandwidth of 1 nm, and response time of 1 sec, using a single accumulation). SERS analysis was conducted on confocal DXR2 Raman microscopy system (Thermo Fisher Scientific, Madison, WI), which includes a red laser source unit (633 nm@70 mW single-frequency laser diode ROUSB-633-PLR-70-1, Ondax, CA), a Plan N oil immersion 100× (Na = 1.25) Olympus objective lens, which provides a sub-micrometer XY spatial resolution and produces a low background signal. Laser power on the sample does not exceed 1 mW and the accumulation time was ≈1s. The polymer and nanocomposite films were deposited on coverslips, with a water layer above the samples to avoid overheating. The High Resolution Transmission Electron Microscopy (HRTEM) analysis of the nanocomposites employed a JEOL JEM 2010 HR Transmission electron microscope and the SEM analysis employed a Hitachi SU70 Scanning electron microscope with X-ray microanalysis (detector-background secondary electron detector (BSE) with 14 mm and 15.7 mm aperture). The AFM imaging was done on an OmegaScope-R scanning probe microscope (AIST-NT Inc.) in tapping mode at 0.2 Hz scanning speed. The POM analysis was performed on a Nikon Optiphot 150 incident light DIC microscope using polarizers crossed at 90°. Fourier Transform infrared (FTIR) Spectroscopy analysis was recorded on a PerkinElmer Spectrum Two Fourier Transform Infrared system from a wavenumber range of 4000 to 500 nm^{-1}. The XPS analysis was performed using a Thermo Scientific Nexsa G2 spectrometer with operating pressure ≈1 × 10^{-9} Torr. A hemispherical analyzer determined electron kinetic energy, using a pass energy of 200 eV for wide/survey scans, and 50 eV for high-resolution scans. XRD spectra were recorded on Rigaku XtaLAB Synergy-S equipped with a HyPix-6000HE hybrid photon counting area detector. Powder diffraction experiments were performed using a Cu-target PhotonJet-S source with divergence slits set to provide a 1.2 mrad beam. A Gandolfi data collection strategy (simultaneously scanning φ and ω) at a single κ orientation was used. Three detector positions were used to collect data to 90° in 2Θ at a detector distance of 60 mm. The samples were loaded on a Kapton loop using paratone oil, and the beam was focused on a small amount of the sample for XRD measurements.

We previously showed[5h] that PF8TTS (M$_n$ = 30 000 Da) has the highest CD signal in the visible region among a series of similar polymers. In this work, we aimed to enhance the chiroptical response by combining this polymer with plasmonic nanostructures. The synthetic route and the respective characterization techniques were described previously.[5h] Here, we will be referring to the PF8TTS polymer as P*, polymer-Au nanoparticle hybrids as P*AuNPs, and polymer-Au nanostar hybrid as P*AuNSs.

Initially, we synthesized a series of nanoformulations with polymer P* and gold nanoparticles to see the effect of plasmonic activity on our chiral polymer. P* was used as a ligand to coat our AuNPs in an in situ technique. We prepared formulations with polymer:gold precursor mass ratios of 1:0.5, 1:1, 1:1.5, and 1:3. The synthesis protocol used for the 1:1 mass ratio nano formulation which yielded the best results are described below, and the synthesis protocols for the other formulations are described in the supplementary information (Section S1, Supporting Information).

2.3. P*AuNPs 1:1

A total of 270 mg of TOAB was dissolved in 8 mL toluene and stirred at 800 rpm (rotations per minute) for 2 min. A solution of 10 mg of HAuCl$_4$.3H$_2$O in 3 mL DI water was then added. The two-phase system (organic top layer and aqueous bottom layer) was stirred at 500 rpm. The rapid change of the organic layer to an orange color as the aqueous layer became transparent indicated the transfer of the gold precursor to the organic layer. Next, a solution of 10 mg of P* in 3 mL of toluene was added to the 2-phase system. The organic phase changed to a greenish-orange color. Next, 378.3 mg of NaBH$_4$ was dissolved in 2.5 mL of DI water and added to the mixture, further reducing Au^{3+} to Au^0 nanoparticles. Upon reduction, the color of the organic layer exhibited a reddish-brown tinge.[11] The organic layer was then carefully extracted. The nanocomposite was precipitated using chilled ethanol. The precipitate was collected via centrifugation, washed with ethanol 4–5 times, dried, and stored in a vacuum. An illustration of the synthesis scheme of P*AuNPs nanocomposite is provided in Figure S1A (Supporting Information).

2.4. P*AuNSs 1:2

The nanocomposites with gold nanostars were synthesized by the galvanic replacement of copper seeds with gold in an in situ fashion.[12] We produced these in polymer: gold precursor mass ratios of 1:1, 1:2, 1:4, and 1:12. The synthesis protocol for the 1:2 formulation which yielded the best results is described below, and the corresponding protocols for the other formulations are provided (Section S1, Supporting Information).

Initially, 9.9 mg of CuCl(I) was added to 5 mL of oleylamine in an inert atmosphere in a three-necked round bottom flask. The

mixture was sealed, heated to 100 °C, and stirred at 500 rpm for 30 min. The temperature was further increased to 205 °C, and the mixture developed a light-yellow color indicating the formation of copper complexes. The mixture was stirred at 200 rpm for 5 min. It was then cooled to 80 °C and a solution containing 60 mg of $HAuCl_4 \cdot 3H_2O$, 1 mL oleylamine, and 4 mL toluene was added immediately to the round bottom flask. The solution instantly changed to a reddish-orange color. The mixture was stirred at 200 rpm for 2 min and then stopped. The mixture was left to age at 60 °C for 45 min. Next, a solution containing 30 mg P* in 2 mL toluene was added slowly to the flask. The mixture developed a dark greenish tinge upon adding the polymer solution. It was left to age for 2 h at 60 °C.[12] At the end of the reaction, the mixture was allowed to cool and was then precipitated with chilled ethanol. The precipitated P*AuNS hybrid nanocomposites were collected by centrifugation and washed with ethanol 4–5 times. The final nanocomposite was dried and stored in a vacuum. A schematic illustration of the synthesis of P*AuNSs nanocomposite is provided in Figure S1B (Supporting Information).

The samples were spin-coated onto glass substrates at 750 rpm for 5 min, then dried in a vacuum chamber overnight. The prepared films were then characterized in both pristine and annealed conditions. The annealing process was done in a vacuum oven. The films prepared on glass substrates were used for the ellipticity studies, while the films used for material characterization were coated on silicon substrates with the same spin coating parameters. The molecular structure of the polymer, P*, used in these experiments is shown in **Figure 1A**. A schematic representation of the hybrid nanocomposite films (P*AuNPs and P*AuNSs) before and after spin coating and annealing is provided in Figure 1B,C.

2.5. Plasmon Field Simulations

Full-wave analysis of the optical response of plasmonic nanostars was done using the COMSOL Multiphysics software package. The main results are presented below, with all the technical details provided in Section S20 (Supporting Information).

3. Results and Discussion

In our previous reports,[4f,5h] we showed that thin films of the neat polymer form helical fibers upon annealing. Here, we confirmed that the Au nanostars did not disrupt the helicity of the polymer fibrils using SEM and AFM imaging (Figure S13B Supporting Information and Figure 3D). The polymer-nanostructure hybrid showed a weak CD response in the pristine state but displayed an enhanced CD response after annealing at 120 °C.[5i] Figure 1D–G compares the optical properties of the P*, P*AuNPs, and P*AuNSs films of 100 nm thickness. The annealed P*AuNPs hybrid film showed a 2.32-fold enhancement of CD at 500 nm wavelength (Figure 1D) while the annealed P*AuNSs hybrid film showed a tenfold CD enhancement at 505 nm wavelength when compared to the annealed P* film of similar thickness. The absorbance of the annealed P*, P*AuNPs, and P*AuNSs films is provided in Figure 1E. In addition to the studies of the samples with the
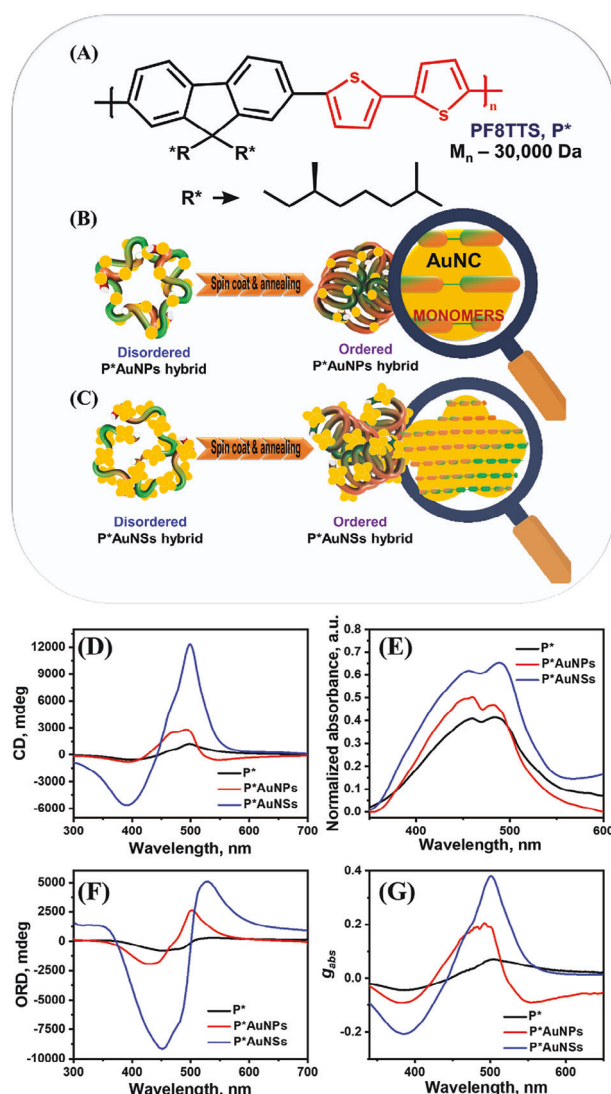

Figure 1. A) Chemical structure of PF8TTS (P*); B) schematic illustration of the structural organization of a P*AuNPs hybrid; C) schematic illustration of the structural organization of P*AuNSs hybrid; D) comparison of CD signals of P*, P*AuNPs, and P*AuNSs annealed films; E) comparison of absorbance of P*, P*AuNPs, and P*AuNSs annealed films; F) comparison of ORD signals of P*, P*AuNPs, and P*AuNSs annealed films; G) comparison of dissymmetry factors of P*, P*AuNPs, and P*AuNSs annealed films. The thickness of all the films (P*, P*AuNPs, P*AuNSs) compared here was 100 nm.

same thickness, we characterized the samples with the same concentration of the polymer, spin-coated at the same rpm. Naturally, the addition of AuNPs and AuNSs resulted in thicker hybrid films, when compared with the thickness of pure polymer film. The annealed P*AuNPs hybrid film showed a sevenfold enhancement of CD (maximum value – 4628 mdeg) at 500 nm wavelength (Figure S2A, Supporting Information) relative to the annealed PF8TTS neat polymer film P* with comparative polymer concentration. The annealed P*AuNSs hybrid film showed a 46-fold CD (maximum value – 29 908 mdeg) enhancement at 505 nm wavelength (Figure S2A, Supporting Information)

**ADVANCED
SCIENCE NEWS**

www.advancedsciencenews.com

**ADVANCED
OPTICAL
MATERIALS**

www.advopticalmat.de

relative to the annealed P* film. The thickness of the polymer film used for comparison here was 80nm and the ellipticity signal of 647 mdeg was observed at 498 nm. The absorbance signals of the annealed P*AuNPs and P*AuNSs films of higher thickness are provided in Figure S2B (Supporting Information). The P*AuNPs hybrid film (250 nm thick) annealed at 120 °C showed ≈1000 times enhancement in CD response (Figure S2E, Supporting Information), while the P*AuNSs hybrid film (263 nm thick) annealed at 120 °C showed an enhancement of the CD response over 4000 times (Figure S2F, Supporting Information) in comparison to their non annealed state. The absorbance peak of the pristine and annealed films for P*AuNPs and P*AuNSs hybrid films are in the same region of the visible spectrum as seen in Figures S2G,H (Supporting Information). Even though the thickness of the hybrid films was more than twice that of the pure polymer film, the total amount of chiral molecules per unit area should be roughly the same. Hence, one might also reasonably compare the films spin-coated from solutions with the same concentration of the polymer to assess the absolute enhancement of the CD and g_{abs}.

Figure 1F shows the difference in the ORD spectra calculated via the Kramers-Kronig transformation of the CD spectrum of the polymer and polymer hybrid films. The ORD spectra show a positive Cotton effect (positive gradient followed by a negative gradient) for all three films. The P*AuNSs spectrum displayed the largest ORD maximum of 5109 mdeg at 530 nm and a minimum of 9175 mdeg at 452 nm wavelength. The P*AuNPs spectrum showed a maximum of 2616 mdeg at 502.6 nm and a minimum of 1932 mdeg at 428 nm, while the P* CD spectrum displayed a maximum of 305 mdeg at 536 nm and a minimum of 818 mdeg at 455 nm. Notably, the ORD signal of the P*AuNSs sample remained high at wavelengths far from the resonance absorption wavelength. The ORD signals for P*AuNPs and P*AuNSs of 250 nm and 263 nm film thicknesses respectively are compared in Figure S2D (Supporting Information). Figure 1G compares the absorption dissymmetry factors of P*, P*AuNPs, and P*AuNSs films at 100 nm thickness, showing a 2.5-fold enhancement in the maximum g_{abs} of P*AuNPs (0.205) and 4.6-fold enhancement in the maximum g_{abs} of the P*AuNSs (0.38) compared to the neat annealed polymer film (0.07). The maximum g_{abs} of P*AuNPs and P*AuNSs at 250nm and 263 nm film thickness were 0.25 and 0.64 respectively (Figure S2C, Supporting Information). Magnified CD spectra of the unannealed P*AuNPs and P*AuNSs hybrid films are presented in Figure S3A,B (Supporting Information). Magnified CD and ORD spectra of the annealed P*AuNPs and P*AuNSs film are in Figure S3C–F (Supporting Information). The CD spectra rapidly decay after peaking at the resonant wavelengths. However, the CD signal of P*AuNSs remained higher (≈1000 mdeg) than that of P*AuNPs in the longer wavelength region. To exclude possible effects of linear dichroism (LD) on the observed data, we also measured LD spectra of P*, P*AuNPs, and P*AuNSs films at 100nm thickness (Figure S4, Supporting Information). This showed that LD response was negligible compared to CD response in these samples. Both the nanocomposites displayed consistent optical signals post-annealing as long as the nanocomposites were stored under proper vacuum conditions.

We varied the polymer-to-gold ratio in each system to maximize CD response, and the results are shown in Figure S7 (Sup-

porting Information). Among the different polymer-to-gold precursor mass ratios, P*AuNPs 1:1 and P*AuNSs 1:2 displayed the highest ellipticity. All hybrid films that were annealed at 120 °C displayed higher ellipticity than films annealed at higher or lower temperatures. The highest CD signal (CD_{max}) for each polymer-to-gold ratio of P*AuNPs and P*AuNSs hybrid films is presented in **Figure 2A**. A detailed analysis showing the trend of the ellipticity and the dissymmetry ratios of the P*AuNPs and P*AuNSs hybrids with varying polymer-to-gold ratios is presented in Figures S7A–D (Supporting Information). We also varied the annealing temperature for the P*AuNPs and P*AuNSs hybrid films at 25, 100, 120, 150, and 175 °C. Results for the neat polymer were previously reported.[5h,i] As reported by Oh et al., upon annealing at higher temperatures (>120 °C), the nanoparticles embedded in the polymer fibrils were observed to aggregate, reducing the CD response.[4f] Our hybrids also showed the highest ellipticity and g_{abs} at 120 °C. Variation of the maximum ellipticity for P*, P*AuNPs, and P*AuNSs with annealing temperature is presented in Figure 2B. At 150 and 175 °C, the P*AuNPs hybrids got destabilized showing reduced ellipticity values (Figure S8A, Supporting Information). For P*AuNSs annealed at temperatures >150 °C, the CD signal significantly decreased, possibly indicating the destabilization of the polymer-AuNSs hybrid. However, at 150 °C, the CD signal was still quite high, reaching 18000 mdeg at 509 nm wavelength (Figure S8B, Supporting Information). We also probed the effect of film thickness for both P*AuNPs and P*AuNSs hybrids, finding that the ellipticity and g_{abs} values increased with increasing thickness of the films (Figure S9A–D, Supporting Information). The g_{abs} maximum values for different thicknesses are compared in Figure 2C. According to Meijer et al.,[2a] the thickness dependence of the dissymmetry factor can be explained by "pseudo" circular dichroism arising from partial conversion of circularly polarized light to linear polarization in high optical density samples with large linear birefringence. In such samples, power or even exponential dependence can be observed, with the dissymmetry factor reaching 1. However, in our case, we believe that the linear thickness dependence of g_{abs} for the P*AuNSs hybrid (Figure 2C; Figure S9D, Supporting Information) arises from the thickness-dependent film morphology. In other words, for a specific film thickness, the value of g_{abs} is dictated by "true" circular dichroism originating from the helicity of the polymeric strands, that are compressed in thinner samples but reach their relaxed helical morphology in thicker films. The thickness of 250 nm corresponds to the helical pitch of the polymer which further supports our conclusion. Also note that the thickness dependence for the P*AuNPs hybrid is very weak in the range from 100 to 250 nm, with the thinnest sample of 80 nm showing a much smaller value of g_{abs} (Figure 2C; Figure S9C, Supporting Information), which again is consistent with the compression of the fibrils. In Figure 2D, we summarized the highest g_{abs} and CD values observed for the P*AuNPs and P*AuNSs films (both the 100 and ≈250 nm thick films). Table S1 (Supporting Information) compares our g_{abs} value to those previously reported for similar systems.

We further characterized these hybrid nanocomposite films to understand the role of plasmonic nanostructures in enhancing the chiroptical response of the polymer. Previously, Zhai et. al. reported a one-pot synthesis of in situ polythiophene-stabilized gold nanoparticles using an approach similar to that employed
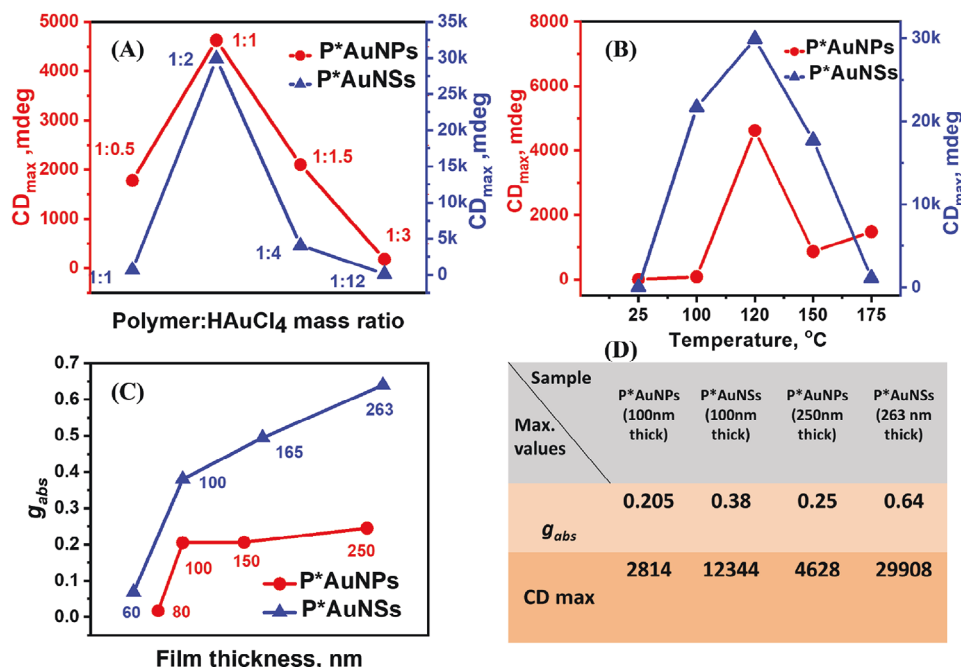
Figure 2. A) Polymer:gold precursor mass ratio optimization for P*AuNPs and P*AuNSs; B) dependence of CD_{max} on annealing temperature for P*AuNPs, and P*AuNSs; C) film thickness dependence of CD_{max} for P*AuNPs and P*AuNSs; D) tabulated comparison of CD_{max} and g_{max} values of P*AuNPs and P*AuNSs.

here.[11] They found that increasing the amount of the polymer beyond an optimal concentration resulted in nanoparticle fusion or growth. TEM images of the Au NPs in our P*AuNPs composites for the different polymer-to-gold mass ratios are provided in Figure S10 (Supporting Information), showing the variation of size with the polymer: gold ratio. A representative TEM image of P*AuNPs with an inset representing the HRTEM image of the composite is shown in **Figure 3A**. The nanoparticles were reasonably monodispersed and ≈4 nm in diameter. Zhu et. al. reported the organic phase synthesis of multi-branched gold nanocrystals, which was the basis for our AuNS synthesis.[12] In this method, the galvanic replacement of Cu seeds with Au⁰ triggered the formation of gold nanostars via the formation of penta-twinned seed particles. TEM images of P*AuNSs hybrids with varied polymer-to-gold ratios are provided in Figure S11 (Supporting Information). A representative TEM image of P*AuNSs with an inset showing a higher-magnification image of the polymer-coupled AuNSs is provided in Figure 3B. As shown here, some of the gold nanostructures have grown into multibranched Au nanostars with characteristic overall dimensions of up to 150 nm, while others remain relatively small penta-twinned nanostructures with very short arms. Nanostars with 3–5 fully-grown arms were observed in the TEM images, similar to those previously reported.[12] The arm-to-arm length of the full-grown nanostars ranged from 120–150nm. We also observed partially grown nanostars with arm-to-arm lengths of 75–90nm, and multi-twinned Au nanostructures with high curvature surfaces and overall size ranging from 20–25nm (Figure S12A–D, Supporting Information). Multiple domains are evident in the TEM images showing the characteristic penta-twinned structure (Figure S12D, Supporting Information). These

differently branched Au nanostructures were observed on the same TEM grid that was prepared via drop-casting a dilute dispersion of P*AuNSs to achieve the low coverage needed for TEM imaging, which was not annealed. Note that the degree of aggregation and segregation by size and shape observed in the TEM images is not observed in the spin-cast and annealed nanocomposite thin films examined by AFM. Rather, the aggregation and size segregation are artifacts of the sample preparation method required for TEM imaging. Figure S13A,B (Supporting Information) shows SEM images of annealed P*AuNPs and P*AuNSs films, respectively.

A uniform distribution of the nanostructures on the polymer fibrils can be seen as bright spots in the SEM images. For the P*AuNPs film (Figure S13A, Supporting Information), the size of Au nanoparticles was too small to resolve the annealed P* helical fibrils. In Figure 3C,D, we present AFM images of P*AuNPs and P*AuNSs hybrid films spin-coated on adhesion glass slides. The nanostructures in both cases are well distributed on the P* framework. Spherical uniform shapes of individual AuNPs and some parts of irregularly shaped AuNSs, including spikes, were observed in the AFM images. The thickness profiles (along the white arrows) of the P*AuNPs and P*AuNSs hybrids are provided in the insets in Figure 3C,D respectively. The P*AuNPs hybrid height profile indicates the size of a single nanoparticle embedded on the top of polymer fibrils, and the height profile of P*AuNSs gives an idea of different sizes of spikes ranging from 10–30 nm. The height profiles from AFM images are not expected to provide exact information on the sizes of the nanostructures when they are embedded in a polymer matrix, because AFM topography is representative of the whole hybrid structure. The diameters of a polymer fibril and AuNPs are comparable
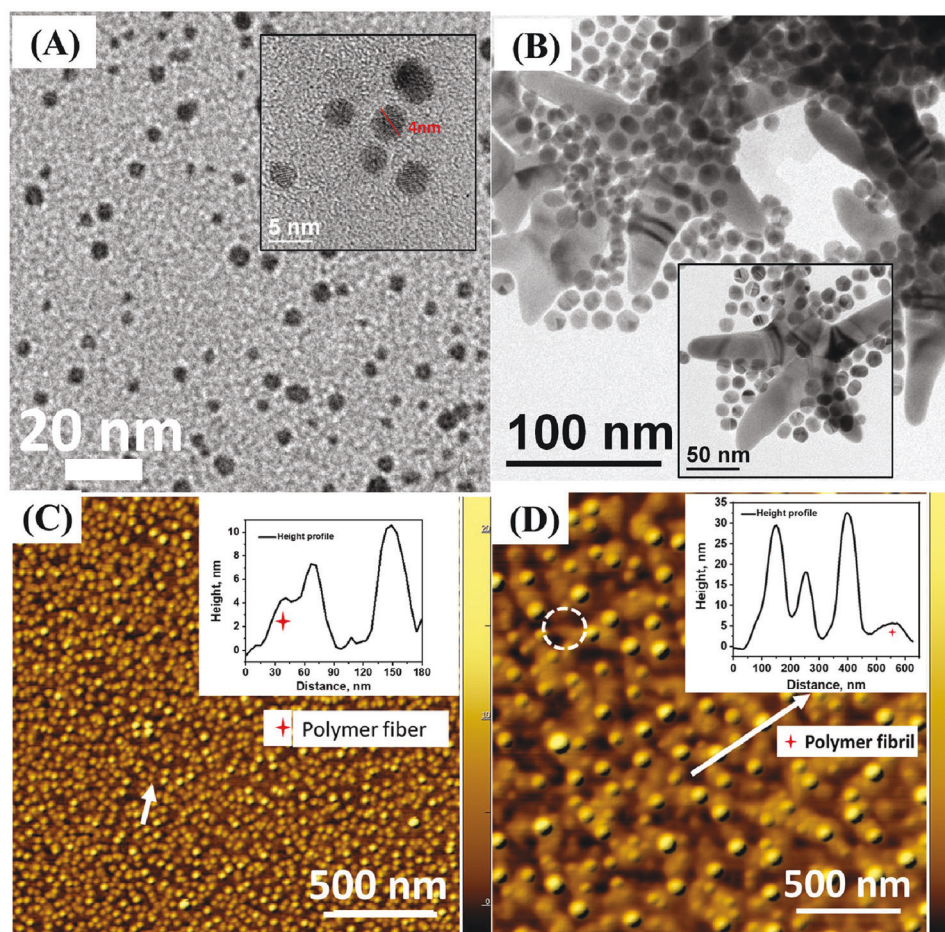
**ADVANCED
SCIENCE NEWS**

www.advancedsciencenews.com

**ADVANCED
OPTICAL
MATERIALS**

www.advopticalmat.de

Figure 3. A) TEM image of P*AuNPs with an HRTEM image of Au nanoparticles in P* in the inset; B) TEM image of P*AuNSs composite with an HRTEM image of a single grown star with some multi-twinned AuNS in P*; C) AFM images of P*AuNPs film; D) AFM image of P*AuNSs film. A polymer fibril has been circled in white. Figure S14 (Supporting Information) shows magnified AFM images in better contrasts highlighting the polymer fibril.

while AuNSs are larger in size. The magnified AFM images (Figure S14, Supporting Information) show the polymer fibrils with the Au nanocrystals uniformly arranged along them, avoiding any clustering. AFM images of both hybrids indicate that the nanocrystals were embedded well in the polymer fibrils using the in situ synthesis approach, although the patterns of attachment with polymer fibrils were different. The circular birefringence of the annealed P*AuNPs and P*AuNSs hybrids is evident in the polarized optical microscopy (POM) images in Figure S13 (Supporting Information). Polarized optical microscopy visualizes birefringent properties of anisotropic media using image contrast and color changes. The pristine films in Figure S13C-D (Supporting Information) show minimal birefringence in certain areas due to the presence of crystalline mesophase in P*AuNPs and P*AuNSs respectively. In contrast, the POM images in Figure S13E-D (Supporting Information) clearly show multiple areas with birefringence after annealing the P*AuNPs and P*AuNSs film respectively. The elemental composition of the P*AuNPs and P*AuNSs hybrids is summarized in Table S2 (Supporting Information). For the P*AuNSs hybrid, the concentration % of Cu was <0.5% which indicates that most of the copper precursor was replaced during AuNS formation. Additionally, incor-

porating the polymer P* near the end of the reaction ensures that the polymer fibrils attach to the fully converted AuNSs.

Electromagnetic full-wave analysis of the plasmon field confirmed that the local electric field at the surface contained between the nanostars' arms is enhanced relative to the local field at the surface of 4 nm diameter spherical nanoparticles (**Figure 4**). In simulations, we set the tip-to-tip length of a penta-twinned nanostar to 20 nm and varied the aspect ratio of the ellipsoidal arms (longer semi-axis to shorter semi-axis) from 10 to 20. These parameters were selected as partial representations of the range of sizes and aspect ratios of nanostars present in the system (Figure 3B; Figure S12, Supporting Information). Because evaluating the preferred positioning of nanostars inside the thin film samples was not feasible, we simulated the plasmon field for AuNSs oriented both vertically and horizontally with respect to the film surface (vertical orientation refers to the plane that contains the long axes of constituting ellipsoids being perpendicular to the film surface, whereas horizontal orientation refers to that plane being parallel with the surface). The calculated results were then averaged over these two main orientations. The surface averaged electric field (Figure 4A) is the highest for the AuNS with the arms' aspect ratio of 20 in the spectral region ≈500 nm, where
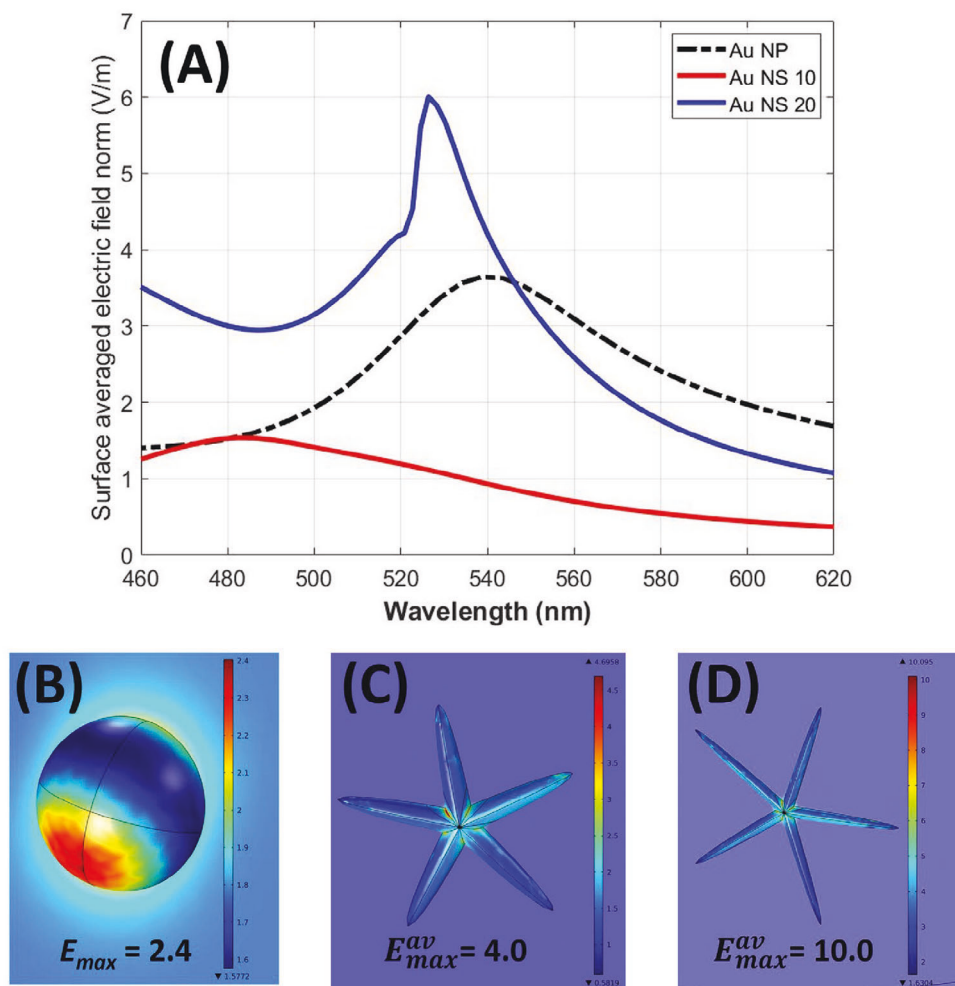
**ADVANCED
SCIENCE NEWS**

www.advancedsciencenews.com

**ADVANCED
OPTICAL
MATERIALS**

www.advopticalmat.de

Figure 4. A) Spectra of the relative surface averaged electric field norm of penta-twinned AuNSs with two different aspect ratios of ellipsoidal arms in comparison with a 4 nm diameter AuNP, averaged over AuNSs' orientation with respect to the film surface; B) electric field enhancement map at the surface of 4 nm diameter AuNP, measured at 500 nm excitation wavelength; C) electric field enhancement map at the surface of a penta-twinned AuNS with the aspect ratio of 10 and oriented parallel to the film surface, measured at 505 nm excitation wavelength; D) electric field enhancement map at the surface of a penta-twinned AuNS with the aspect ratio of 20 and oriented parallel to the film surface, measured at 505 nm excitation wavelength.

the experimental plots show the enhancement of absorbance and CD (Figure 1D-E). At the same time, the surface averaged electric field for AuNSs with the arms' aspect ratio of 10 is found to be smaller than that of AuNPs. The maximum local field enhancement factors differ significantly for the spherical nanoparticle and the nanostars, showing the largest value for the AuNSs with an aspect ratio of 20 (Figure 4B–D). The local electric field at the surface tends to reach its maximum in the crevices between the arms (plasmonic hot spots, Figure 4C,D), whereas for a spherical nanoparticle the field peaks at the larger areas around the poles (Figure 4B). This is notable because even pentatwinned structures with very short arms may have high-curvature crevices between the arms along grain boundaries. Surface averaging results in a lower relative field of nanostars with an aspect ratio of 10 as compared to the spherical NPs, because they have the higher curvature (smaller radius of curvature) of the higher aspect-ratio stars. The highest value of the enhancement factor is found for the aspect ratio of 20 (Figure 4D). For the AuNSs these values were estimated at the excitation wavelength of 505 nm, which

corresponds to the maximum observed CD of the P*AuNSs annealed thin film sample. The experimentally measured ratio of CD enhancement for P*AuNSs and P*AuNPs annealed samples is 4.31 in the case of 100 nm thick films, whereas the simulated ratio of the averaged local electric field enhancement factors at the surfaces of the nanostars with the aspect ratio of 20 and the 4 nm diameter nanosphere is 4.17, which is remarkably close to the experiment. It is also worth noting that the simulated surface averaged electric field for the AuNSs peaks was at around 525 nm. Thus, the high curvature and presence of plasmonic hotspots observed in the simulations somehow capture the range of aspect ratios and local curvatures observed in the polydisperse nanostar materials, even though the experimental structures differ from the idealized nanostar shapes of the simulations. Therefore, it seems that further enhancement of chiroptical properties can be achieved for a polymer with a red-shifted CD maximum, which will be the scope of our future work.

To validate the synthesis of desired nanocomposites for this study, we subjected them to various characterization
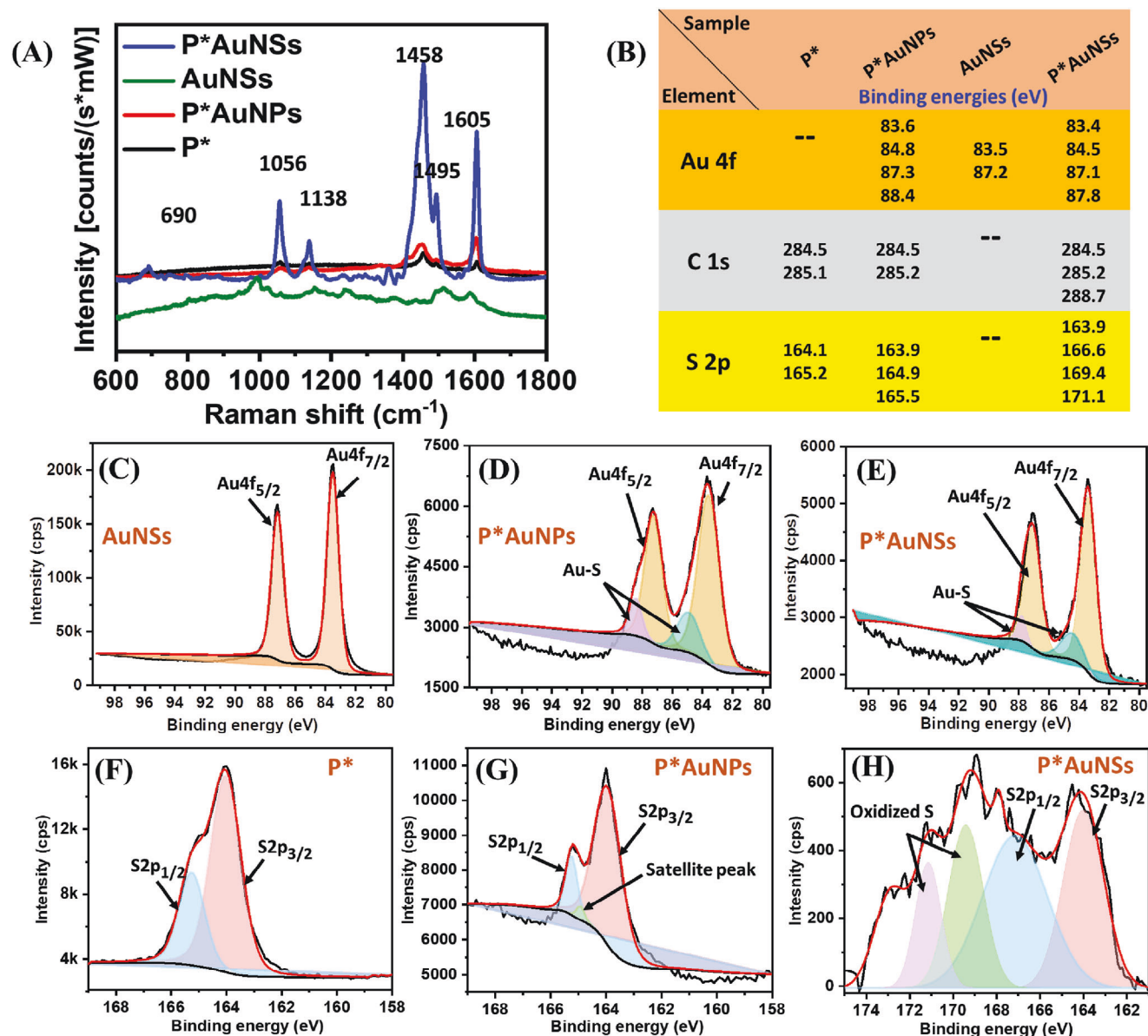
ADVANCED
SCIENCE NEWS

www.advancedsciencenews.com

ADVANCED
OPTICAL
MATERIALS

www.advopticalmat.de

Figure 5. A) Raman spectra of P*, P*AuNPs, P*AuNSs, and AuNSs; B) a table summarizing the binding energies for Au 4f, C 1s, and S 2p orbitals; C) XPS spectrum of AuNS in the Au 4f region, showing the metallic Au $4f_{5/2}$ and Au $4f_{7/2}$; D) XPS spectrum of P*AuNPs in the Au 4f region, showing the metallic Au $4f_{5/2}$ and Au $4f_{7/2}$ and corresponding Au-S peaks; E) XPS spectrum of P*AuNSs in the Au 4f region, showing the metallic Au $4f_{5/2}$ and Au $4f_{7/2}$ and corresponding Au-S peaks; F) XPS plot of P* in the S2p region showing the $S2p_{1/2}$ and $S2p_{3/2}$ peaks; G) XPS plot of S2p for P*AuNPs in the S2p region showing the $S2p_{1/2}$, $S2p_{3/2}$ and a new satellite peak; H) XPS plot of S2p for P*AuNSs in the S2p region showing the $S2p_{1/2}$, $S2p_{3/2}$ and two new satellite peaks.

(XRD, Raman, FTIR, and XPS) techniques. The phase formation for each as-synthesized nanocomposite was verified by X-ray diffraction study, where regular peaks for polymer and gold nanostructures individually were observed. The XRD patterns (Figure S16A, Supporting Information) show sharp crystalline gold peaks in P*AuNPs and P*AuNSs in addition to the broad peaks from PF8TTS. Peaks at 2θ values of 37.82°, 44.06°, 64.42° and 77.53° can be assigned to (111), (200), (220), and (311) planes of gold, respectively which are well matched with the previous reports for AuNP.[13] The peaks corresponding to d-spacings of 14Å @2θ = 6°, 8Å @2θ = 12°, and 4.7Å @2θ = 19° are the

semi-crystalline polymer peaks in the annealed pure and hybrid films.[5i] Thus, the nanocomposites showed peaks from both the polymer and gold nanocrystals which indicates that the semicrystalline nature of polymer chains was not affected by neither the isotropic nor anisotropic Au nanocrystals. Further, Raman spectral analysis verified the change in vibrational modes after the composite formation with AuNPs and AuNSs respectively (**Figure 5A**). A Raman shift (10 cm^{-1}) and enhancement (2.44-fold) at 690 cm^{-1} corresponds to the interaction of AuNSs with the C—S—C deformation mode of polymer.[5i] A fivefold enhancement at 1056 cm^{-1} can be attributed to the SERS associated with

the C—S ring stretch and the gold surface of AuNSs.[14] Furthermore, the peak at 1138 cm^{-1} (C—C inter-ring stretch) was also enhanced by 2.6 folds due to the SERS effect.[5i] The major enhancement (≈9-folds) at 1458 cm^{-1} (C—C stretch, C—H bending in ring plane) and 1495 cm^{-1} (CH$_3$ deformation) depicts the maximum SERS in P*AuNSs composite.[15] Moreover, the peak at 1605 cm^{-1} corresponds to the C=C symmetric stretch in the polymer matrix.[15b] Based on the comparative analogy (1056, 1138, 1458, and 1605 cm^{-1}), it is quite evident that the SERS was more prominent in P*AuNSs when compared to P*AuNPs. Thus, the SERS enhancement seen here aligns with the trend observed in our chiroptical studies. Vibrational spectroscopy studies (FTIR) of P*, P*AuNPs, and P*AuNSs annealed films showed no notable difference between the polymer and the hybrid films (Figure S16B, Supporting Information). The peaks between 3060 and 2860 cm^{-1} are from aromatic and aliphatic C—H stretches.[16] The peaks between 1625 and 1489 cm^{-1} arise from symmetric in plane C=C stretching and aromatic C—C stretching respectively, while the peak between 1350 and 1100 cm^{-1} can be assigned to C—H bending and C—C inter ring stretch.[5h,i,16b] The peaks at 730 cm^{-1} represent the out of plane aromatic C—H bending while the peak at 570 cm^{-1} is from C—S bending.[5h]

The interactions between the chiral polymer and plasmonic nanostructures were further probed using XPS analysis of nanocomposites. High-resolution scans in the Au4f, C1s, and S2p energy ranges were measured. The observed changes in the binding energy values of the polymer and the nanocomposites in Au4f, S2p, and C1s are summarized in Figure 5B. In the case Au4f range, the AuNSs (Figure 5C) exhibit sharp peaks at 83.5 and 87.2 eV corresponding to Au4f$_{7/2}$ and Au4f$_{5/2}$ orbitals. In Figure 5D,E, both the composites (P*AuNPs and P*AuNSs) show peaks at 84.8, 84.5, 88.4, and 87.8 eV. The additional peaks are attributed to Au-S interactions associated with the binding of the polymer directly to the gold surface.[17] The S2p for P* in Figure 5F reveals S2p$_{1/2}$ and S2p$_{3/2}$ at 165.2 and 164.1 eV, respectively. The additional satellite peaks at 164.9 eV for P*AuNPs and at 169.4 and 171.1 eV for P*AuNSs (Figure 5G,H) indicate a change in binding energy due to the coordination of thiophene sulfur atoms in the polymer with the gold nanostructures. Additionally, oxidized "SO$_x$" was evident in P*AuNSs due to the oxidative surface of Au nanostructures.[17b,c] Further, the C1s profile for P*, P*AuNPs, and P*AuNSs shows common peaks at 284.5 and 285.2 eV which correspond to sp^2 aromatic (C=C) and sp^3 (C-S) from the framework (fluorene and thiophene) of the polymer (Figure S17A–C, Supporting Information).[18] In comparison to polymer, the P*AuNSs and P*AuNPs exhibit a higher sp^2 to sp^3 ratio which indicates the interaction of C—S as well as C=C bond on gold nanosurface after nanocomposite formation. Thus, the interaction of gold nanostructures with the polymer at the surface vicinity was substantially evident from the Raman and XPS analysis.

4. Conclusion

To conclude, we show that in situ incorporation of Au nanostars into a chiral polymer resulted in a giant enhancement of circular dichroism and circular birefringence for the first time. The annealed polymer-gold nanostar hybrid showed a 46-fold augmented ellipticity relative to the annealed neat chiral polymer film and >10^3-fold enhancement of ellipticity relative to its unannealed state. The optimized nanocomposite also showed an absorption dissymmetry factor of 0.64 – an exceptionally high value that may render this type of material suitable for device applications, such as fabricating thin film-based components for integrated photonics. Relative to a nanocomposite using the same polymer doped with traditional spherical gold nanoparticles, the polymer-gold nanostar yielded a peak CD value almost 7 times greater. This was ascribed to the formation of plasmonic hot spots at the tips of the nanostars' arms, as confirmed by plasmon field simulations. This was additionally tested via Raman microspectroscopy, which revealed surface-enhanced Raman scattering (SERS) in the nanocomposites. XRD showed characteristic crystalline peaks of gold within the nanocomposite. XPS analysis provided clear evidence of close contact interactions of the polymer fibrils with the AuNSs. Electron microscopy showed a uniform distribution of the plasmonic nanocrystals in the polymer. Although the incorporation of plasmonic nanoparticles into chiral media has been studied previously, the concept of in situ incorporation of anisotropic nanocrystals (nanostars) with many plasmonic field hot spots has not been explored to date. Our work showed, for the first time, a realistic pathway to real-life thin film integrated photonic devices that harness giant amplification of chiroptical properties of hybrid organic: inorganic materials.

Supporting Information

Supporting Information is available from the Wiley Online Library or from the author.

Conflict of Interest

The authors declare no conflict of interest.

Data Availability Statement

The data that support the findings of this study are available in the supplementary material of this article.

**ADVANCED
SCIENCE NEWS**

www.advancedsciencenews.com

**ADVANCED
OPTICAL
MATERIALS**

www.advopticalmat.de

[1] a) A. O. Govorov, Y. K. Gun'ko, J. M. Slocik, V. A. Gérard, Z. Fan, R. R. Naik, *J. Mater. Chem.* **2011**, *21*, 16806; b) D. Vila-Liarte, N. A. Kotov, L. M. Liz-Marzán, *Chem. Sci.* **2022**, *13*, 595.

[2] a) M. R. Craig, P. Jonkheijm, S. C. J. Meskers, A. P. H. J. Schenning, E. W. Meijer, *Adv. Mater.* **2003**, *15*, 1435; b) J. L. Greenfield, J. Wade, J. R. Brandt, X. Shi, T. J. Penfold, M. J. Fuchter, *Chem. Sci.* **2021**, *12*, 8589; c) X. Wang, Z. Tang, *Small 13*, 1601115; d) T. Kyu, N. Yasuda, M. Tabushi, S. Nomura, H. Kawai, *Polymer Journal* **1975**, *7*, 108; e) K. J. Smith Jr., *J. Polym. Sci., Polym. Phys. Ed.* **1968**, *6*, 1723; f) R. Wilks, N. D. Hughes, R. J. Hicken, *J. Phys.: Condens. Matter* **2003**, *15*, 5129.

[3] a) V. K. Valev, J. J. Baumberg, C. Sibilia, T. Verbiest, *Adv. Mater.* **2013**, *25*, 2517; b) G. Albano, G. Pescitelli, L. Di Bari, *Chem. Rev.* **2020**, *120*, 10145.

[4] a) R. Abbel, A. P. H. J. Schenning, E. W. Meijer, *Macromolecules* **2008**, *41*, 7497; b) E. Peeters, M. P. T. Christiaans, R. A. J. Janssen, H. F. M. Schoo, H. P. J. M. Dekkers, E. W. Meijer, *J. Am. Chem. Soc.* **1997**, *119*, 9909; c) C. Kulkarni, S. C. J. Meskers, A. R. A. Palmans, E. W. Meijer, *Macromolecules* **2018**, *51*, 5883; d) J. Wade, J. N. Hilfiker, J. R. Brandt, L. Liirò-Peluso, L. Wan, X. Shi, F. Salerno, S. T. J. Ryan, S. Schöche, O. Arteaga, T. Jávorfi, G. Siligardi, C. Wang, D. B. Amabilino, P. H. Beton, A. J. Campbell, M. J. Fuchter, *Nat. Commun.* **2020**, *11*, 6137; e) B. Nowacki, C. Oh, C. Zanlorenzi, H. Jee, A. Baev, P. N. Prasad, L. Akcelrud, *Macromolecules* **2013**, *46*, 7158; f) H. S. Oh, S. Liu, H. Jee, A. Baev, M. T. Swihart, P. N. Prasad, *J. Am. Chem. Soc.* **2010**, *132*, 17346; g) H. S. Oh, H. Jee, A. Baev, M. T. Swihart, P. N. Prasad, *Adv. Funct. Mater.* **2012**, *22*, 5074; h) H. S. Oh, G. S. He, W.-C. Law, A. Baev, H. Jee, X. Liu, A. Urbas, C.-W. Lee, B. L. Choi, M. T. Swihart, P. N. Prasad, *Adv. Mater.* **2014**, *26*, 1607; i) C.-K. Lim, M. J. Cho, A. Singh, Q. Li, W. J. Kim, H. S. Jee, K. L. Fillman, S. H. Carpenter, M. L. Neidig, A. Baev, M. T. Swihart, P. N. Prasad, *Nano Lett.* **2016**, *16*, 5451; j) G. S. He, M. J. Cho, W. J. Kim, A. Baev, M. T. Swihart, P. N. Prasad, *Adv. Opt. Mater.* **2013**, *1*, 763; k) C. Kulkarni, M. H. C. van Son, D. Di Nuzzo, S. C. J. Meskers, A. R. A. Palmans, E. W. Meijer, *Chem. Mater.* **2019**, *31*, 6633; l) B. Laidlaw, J. Eng, J. Wade, X. Shi, F. Salerno, M. J. Fuchter, T. J. Penfold, *Chem. Commun.* **2021**, *57*, 9914.

[5] a) J.-Y. Kim, J. Yeom, G. Zhao, H. Calcaterra, J. Munn, P. Zhang, N. Kotov, *J. Am. Chem. Soc.* **2019**, *141*, 11739; b) J. Cornil, D. Beljonne, J.-P. Calbert, J.-L. Brédas, *Adv. Mater.* **2001**, *13*, 1053; c) P. C. Mondal, N. Kantor-Uriel, S. P. Mathew, F. Tassinari, C. Fontanesi, R. Naaman, *Adv. Mater.* **2015**, *27*, 1924; d) R. Naaman, D. H. Waldeck, *Annu. Rev. Phys. Chem.* **2015**, *66*, 263; e) D. H. Waldeck, R. Naaman, Y. Paltiel, *APL Mater.* **2021**, *9*; f) D. Neher, *Macromol. Rapid Commun.* **2001**, *22*, 1365; g) U. Scherf, E. J. W. List, *Adv. Mater.* **2002**, *14*, 477; h) J. P. Joseph, S. R. Abraham, A. Dutta, A. Baev, M. T. Swihart, P. N. Prasad, *J. Phys. Chem. Lett.* **2022**, *13*, 9085; i) J. P. Joseph, T. Malone, S. R. Abraham, A. Dutta, S. Gupta, A. Kuzmin, A. Baev, M. T. Swihart, J. R. Hendrickson, P. N. Prasad, *Adv. Mater.* **2024**, *36*, 2305684; j) C. Kulkarni, D. Di Nuzzo, E. W. Meijer, S. C. J. Meskers, *J. Phys. Chem.*

B **2017**, *121*, 11520; k) M. Fukuda, R. Rodríguez, Z. Fernández, T. Nishimura, D. Hirose, G. Watanabe, E. Quiñoá, F. Freire, K. Maeda, *Chem. Commun.* **2019**, *55*, 7906; l) S. Huang, H. Yu, Q. Li, *Adv. Sci.* **2021**, *8*, 2002132; m) M. Kang, P. Zhang, H. Cui, S. M. Loverde, *Macromolecules* **2016**, *49*, 994; n) Y. Zhao, N. A. Abdul Rahim, Y. Xia, M. Fujiki, B. Song, Z. Zhang, W. Zhang, X. Zhu, *Macromolecules* **2016**, *49*, 3214; o) S. Li, T. Miao, X. Cheng, Y. Zhao, W. Zhang, X. Zhu, *RSC Adv.* **2019**, *9*, 38257; p) S.-k. Ahn, M. Gopinadhan, P. Deshmukh, R. K. Lakhman, C. O. Osuji, R. M. Kasi, *Soft Matter* **2012**, *8*, 3185; q) C. Kulkarni, R. H. N. Curvers, G. Vantomme, D. J. Broer, A. R. A. Palmans, S. C. J. Meskers, E. W. Meijer, *Adv. Mater.* **2021**, *33*, 2005720; r) W. C. Trogler, *J. Am. Chem. Soc.* **2009**, *131*, 3119; s) X. Cheng, T. Miao, Y. Qian, Z. Zhang, W. Zhang, X. Zhu, *Int. J. Mol. Sci.* **2020**, *21*, 6186; t) K. Watanabe, K. Akagi, *Sci. Technol. Adv. Mater.* **2014**, *15*, 044203; u) T. Nakano, *Polymer Journal* **2010**, *42*, 103.

[6] a) A. O. Govorov, *J. Phys. Chem. C* **2011**, *115*, 7914; b) A. O. Govorov, Z. Fan, *ChemPhysChem* **2012**, *13*, 2551; c) J. P. Joseph, C. Miglani, A. Maulik, S. R. Abraham, A. Dutta, A. Baev, P. N. Prasad, A. Pal, *Angew. Chem., Int. Ed.* **2023**, *62*, 202306751.

[7] a) A. O. Govorov, Z. Fan, P. Hernandez, J. M. Slocik, R. R. Naik, *Nano Lett.* **2010**, *10*, 1374; b) L. A. Warning, A. R. Miandashti, L. A. McCarthy, Q. Zhang, C. F. Landes, S. Link, *ACS Nano* **2021**, *15*, 15538.

[8] a) A. Ben-Moshe, B. M. Maoz, A. O. Govorov, G. Markovich, *Chem. Soc. Rev.* **2013**, *42*, 7028; b) B. Calis, M. Yilmaz, *Colloids Surf. A* **2021**, *622*, 126654.

[9] T. Wu, W. Zhang, R. Wang, X. Zhang, *Nanoscale* **2017**, *9*, 5110.

[10] W. Zhang, T. Wu, R. Wang, X. Zhang, *J. Phys. Chem. C* **2017**, *121*, 666.

[11] L. Zhai, R. D. McCullough, *J. Mater. Chem.* **2004**, *14*, 141.

[12] D. Zhu, Y. Liu, M. Liu, X. Liu, P. N. Prasad, M. T. Swihart, *J. Mater. Chem. B* **2020**, *8*, 5491.

[13] A. K. Roddu, A. W. Wahab, A. Ahmad, P. Taba, I. W. Sutapa, *J. Phys.: Conf. Ser.* **2020**, *1463*, 012008.

[14] a) S.-Y. Chen, J. J. Mock, R. T. Hill, A. Chilkoti, D. R. Smith, A. A. Lazarides, *ACS Nano* **2010**, *4*, 6535; b) C. Matricardi, C. Hanske, J. L. Garcia-Pomar, J. Langer, A. Mihi, L. M. Liz-Marzán, *ACS Nano* **2018**, *12*, 8531.

[15] a) Y. L. Wong, W. C. M. Kang, M. Reyes, J. W. P. Teo, J. C. Y. Kah, *ACS Infect. Dis.* **2020**, *6*, 947; b) F. C. B. Maia, P. B. Miranda, *J. Phys. Chem. C* **2015**, *119*, 7386.

[16] a) G. Li, J.-F. Yin, H. Guo, Z. Wang, Y. Zhang, X. Li, J. Wang, Z. Yin, G.-C. Kuang, *ACS Omega* **2018**, *3*, 7727; b) D. Popovici, A. Diaconu, A. Rotaru, L. Marin, *Polymers* **2019**, *11*, 1562.

[17] a) F. Vitale, I. Fratoddi, C. Battocchio, E. Piscopiello, L. Tapfer, M. V. Russo, G. Polzonetti, C. Giannini, *Nanoscale Res. Lett.* **2011**, *6*, 103; b) Y. Xue, X. Li, H. Li, W. Zhang, *Nat. Commun.* **2014**, *5*, 4348; c) R. K. Das, S. Mohapatra, *J. Mater. Chem. B* **2017**, *5*, 2190.

[18] C. Fontanesi, F. Tassinari, F. Parenti, H. Cohen, P. C. Mondal, V. Kiran, A. Giglia, L. Pasquali, R. Naaman, *Langmuir* **2015**, *31*, 3546.